OPTICA

Third-harmonic generation monitoring of femtosecond-laser-induced in-volume functional modifications

Olivier Bernard,[1,*] Andrea Kraxner,[2] Assim Boukhayma,[2] Jeff A. Squier,[3] Christian Enz,[2] and Yves Bellouard[1]

[1]Galatea Laboratory, IEM, STI, École Polytechnique Fédérale de Lausanne (EPFL), Rue de la Maladière 71b, CH-2002 Neuchâtel, Switzerland
[2]Integrated Circuits Laboratory, IEM, STI, École Polytechnique Fédérale de Lausanne (EPFL), Rue de la Maladière 71b, CH-2002 Neuchâtel, Switzerland
[3]Department of Physics, Colorado School of Mines, Golden, Colorado 80401, USA
*olivier.bernard@epfl.ch

Received 6 February 2023; revised 12 May 2023; accepted 22 May 2023; published 16 June 2023

During the last two decades, ultrafast in-volume laser-based processing of transparent materials has emerged as a key 3D-printing method for manufacturing a variety of complex integrated photonic devices and micro-parts. Yet, identifying suitable laser process parameters for a given substrate remains a tedious, time-consuming task. Using a *single* laser source for both processing and monitoring, we demonstrate a method based on *in situ* full-field third-harmonic generation (THG) microscopy that exploits the properties of a low-noise CMOS imager to rapidly identify the entire processing space, discriminating different types of laser-induced modifications, and extracting incubation laws governing the laser exposure process. Furthermore, we show that full-field THG monitoring is capable of identifying parameters leading to enhanced functional properties, such as laser-enhanced etching selectivity. These findings enable accelerated implementations of laser processes of arbitrarily chosen transparent materials and, due to the rapid acquisition time (>100 FPS) of the imager, closed-loop process control.

https://doi.org/10.1364/OPTICA.486746

1. INTRODUCTION

Optical femtosecond laser amplifiers facilitate, with appropriate focusing optical elements, reaching intensities of several TW cm^{-2}. These intensities can induce nonlinear absorption and trigger a series of events that ultimately locally modifies the material [1]. Such laser-induced modifications can exhibit a variety of morphologies, with some being used as bases for emerging fabrication technologies. Notably, femtosecond-laser-induced nanogratings in bulk fused silica [2–4] show an enhanced wet etching rate, while laser-induced localized densification is the building block for direct-write waveguides.

Full characterization of laser-affected zones (LAZs) remains a tedious, destructive process. It typically includes sectioning the specimen, polishing a surface, and sometimes performing an etching step to reveal the structures before observing the specimen under a microscope. Few methods are available for non-destructive observations. Among them, phase-contrast microscopy and related methods based on retardance measurement are satisfying for observing direct-write optical-index-contrast zones [5–8], but are limited in information and offer only a 2D view of LAZs. Indirect methods, such as observation of the diffractive nature of nanogratings [9] and time-resolved observation of plasma growth and decay into permanent modifications [10] have also been reported. However these methods are not easily implementable, or are specific to one type of modification [11].

As ultrafast laser sources matured, coherent nonlinear microscopy has emerged over the last two decades as a new modality for 3D imaging in general. Among them, third-harmonic generation (THG) is a particularly interesting case in the context of observing LAZs. Endogenous image contrast results with THG: the coherent conversion process efficiency dramatically increases when intense light irradiates optically heterogeneous media [12]. In practice, these conditions can be met using a mW-average power femtosecond laser that is tightly focused (several micrometer spot sizes). Although predominately used for biological microscopy [13], this method can also be used to image LAZs inside transparent materials in three dimensions, as demonstrated in Ref. [14] (see also Refs. [15,16] for a pragmatic implementation of THG microscopy). Previous studies used this method to observe the morphology of laser-written waveguides in glass, as THG is sensitive to spatial variation of the refractive index. These observations remain qualitative and limited to morphological ones [17–19].

THG microscopy is therefore an interesting choice for *in situ* imaging of LAZs in bulk glass. So far, these studies have limited themselves to 3D imaging of the contour of laser-modified zones, with no *a priori* correlation with the nature of the modification

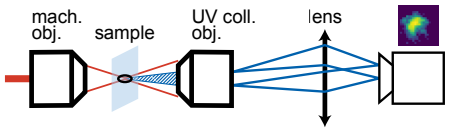

Fig. 1. Working principle of an*in situ*, full-field third-harmonic generation (THG) transmission microscope. A machining pulse modifies the material. Subsequent pulses from the same laser source, but emitted at sub-modification threshold fluences, irradiate the modified area, which results in third harmonic photons generation. The area in focus acts as a diffraction limited source, which is at most the minimum waist of the objective at the focal point. The emitted THG signal is captured with a collection objective and refocused onto a sensor array. A far-field distribution (full-field) of the THG source is thereby retrieved as illustrated.

or, in particular, their functional properties. Furthermore, these studies have focused on exploiting laser scanning arrangements to form a THG image of the modified zones.

This work aims at expanding the capabilities of *in situ* THG as a characterization tool, and as a means to evaluate functional process parameters, including incubation laws, for a given material. As a case study, we focus on a laser–matter exposure regime where self-organized nanostructures form in the bulk of the material. These nanostructures consist of a set of parallel planes, themselves made of an intricate nano-pores network [3,20]. These nano-planes orient themselves along the propagation axis and perpendicular to laser polarization. These anisotropic structures are particularly relevant for numerous applications in 3D manufacturing [21].

Specifically, we explore the information content of the far-field THG intensity distribution thanks to a new type of low-noise CMOS imager capable of few-photon acquisition. Figure 1 pictures the working principle of this method. Far-field THG intensity distribution images correlate with functional properties of the exposed glass. With this method, and using a matrix of dots mapping the relevant laser parameters, we are able to identify not only the modification parameter space for the material, but also singular regions, where accelerated localized etching enhancement is exacerbated.

2. EXPERIMENTAL METHOD

This study has been carried on an adapted femtosecond laser machining platform, illustrated in Fig. 2. A single femtosecond laser source (regenerative Yb-based amplifier, S-pulse HR SP from Amplitude SA) is used. The source, centered at 1030 nm, emits 150 fs pulses at a maximum repetition rate of 100 kHz, and a nominal maximum power of 1 W. An acousto-optic modulator (AOM, MCQ80-A2-L1064-Z32, A. A. Opto-Électronique SA) modulates the processing beam. The beam is expanded to fill the entrance pupil of the machining microscope objective lens (Thorlabs MicroSpot LMH-20X-1064, NA = 0.40). The focal plane lies in the bulk of a 25 mm × 25 mm × 0.25 mm fused silica (Corning 7980 0F) sample. Piezoelectric stages (Mad City Labs, Inc.) move the specimen in a plane perpendicular to the optical axis, while the focusing objective is fixed on a third piezoelectric stage translating along the optical axis. With this configuration, the exposure workspace within the specimen is a 100 µm × 100 µm × 30 µm large parallelepiped.

As the central wavelength of THG for a pump wavelength of 1030 nm is 343 nm, for which usual glass and anti-reflective coatings are often unfit, we developed a custom infinity-corrected,

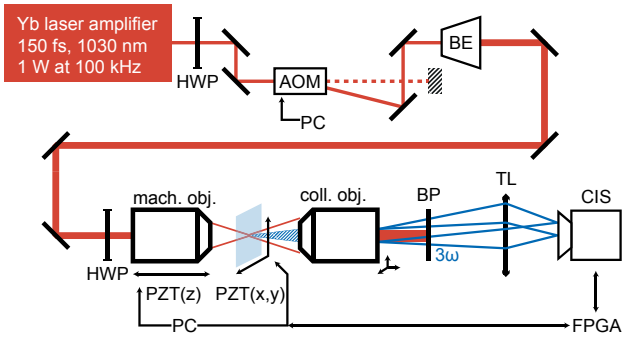

Fig. 2. Schematic of our in-line third-harmonic generation (THG) microscope integrated within a femtosecond laser processing platform. In these experiments, an Yb-regenerative femtosecond laser amplifier delivers the pulses. An external acousto-optic modulator (AOM), connected to a common control unit (PC), modulates the energies. A zero-order half-wave plate (HWP) adjusts the laser polarization state to match the operating requirement of the AOM. The first-order diffracted beam from the AOM is then expanded to fill the machining objective lens' entrance pupil and is tightly focused (NA = 0.4) to achieve a spot diameter of about 2.5 µm in the specimen volume. A glass sample is mounted on a 3D piezoelectric stage (PZT) positioner. During the laser–glass interaction process, THG radiation is generated at the focal spot, and a custom-made infinity-corrected objective lens collects the signal. A filter (BP) rejects the laser excitation wavelength. Finally, a tube lens (TL) focuses the THG signal onto a custom-made CMOS image sensor (CIS), later referred as "imager." A dedicated field programmable gate array (FPGA) controls the imager, itself interfaced with the central control unit (PC).

collection objective lens optimized for 343 nm, based on an arrangement of off-the-shelf fused silica lenses. The collecting objective lens is set on 3D manual translation stages for alignment purposes. Two consecutive narrow bandpass THG filters (Edmund Optics Ltd, BP 343 nm × 5 nm OD4 Ø12.5 mm) filter the collected light. A UV-anti-reflective coating tube lens ($f = 150$ mm) focuses the beam onto our custom-designed CMOS low-noise imager.

This low-noise CMOS imager is based on pinned photodiodes (PPDs) that come with the advantage of good quantum efficiency at lower visible wavelengths (QE ∼ 50%) compared to other image sensor technologies. This makes this sensor technology ideal for the detection of third-harmonic photons generated by probe pulses. Due to its ultra-low noise, the image sensor array achieves photon counting over a full Quarter Video Graphics Array (QVGA) image (320 pixels × 240 pixels) image at a video rate of up to 100 FPS. Its sub-electron noise and high sensitivity allow for short integration times and very low signals, and this, without compromising the dynamic range [22].

The imager exploits an array of 5T pixels based on dual gate PPDs paired with an optimized sense node doping profile, and a low-noise in-pixel source follower design. This, together with column-level amplification and double sampling, ensures sub-electron read noise. Applying a voltage at the sink gate, all charges generated from the photons impinging on the PPDs are dumped. This will be the case for photoelectrons generated outside the probe pulse phase and, particularly, the pump pulse phase that might saturate the sensor. The fact that third-harmonic light generated by consecutive probe pulses can be accumulated in the charge domain without any further processing by defining the integration time is also an advantage. As a result, the number of probe pulse cycles can be tuned for achieving a target signal-to-noise ratio for a given

laser and optical setup, without a penalty on the contrast with background light. Finally, an FPGA device generates the control signals and synchronizes them with the command of the probing source and the data acquisition.

To explore the laser–matter-interaction parameter space, for a given pulse duration, we expose the material over a wide range of pulse fluence values F and number of pulses n. In practice, we write a matrix of dots, with each dot corresponding to a pair of parameters (F, n). This allows the entire experiment to take place in a 100 μm × 100 μm matrix, covering the entire workspace of the piezoelectric stages. Probing LAZs with the same laser beam is done "on the fly," a few milliseconds after the writing of a single dot and using a pulse fluence below the modification threshold.

3. RESULTS AND DISCUSSION

A. Full-Field Tomography versus 3D-Scanning Microscopy

Let us first compare two THG imaging modalities: conventional 3D scanning, hereafter called "scanning mode," and full-field focal-plane tomography, hereafter referred to as "tomographic mode." For both techniques, we use the same array sensor. The LAZ is produced at the origin of the stage coordinate frame. For scanning mode, the 3D image is gathered by summing all values for each scanned position in a cubic volume. For tomographic mode, full-field images are acquired along the z axis only and then stacked together. These methods image a LAZ, processed at $F = 9.72\ \mathrm{J\ cm^{-2}}$ with 14 pulses.

Figure 3 reports the images. Scanning mode reveals an ellipsoid shape, elongated along the optical axis $\vec{e}_z$, typical of nonlinear absorption processes occurring in the bulk of a transparent substrate [23,24]. The width of the ellipsoid is, as expected, about the beam size, 2.5 μm. In tomographic mode, the collection objective is focused so that the image formed on the imager at $\Delta z = 0$ μm is the smallest. The imaging system has a resolution of circa 1 px/μm. See Appendix A for a discussion on the spatial resolution of THG. This mode exhibits a THG signal spread across a much wider area on the imager than for scanning mode. Considering the coherence and directionality of THG, this observation indicates that the medium is optically highly heterogeneous.

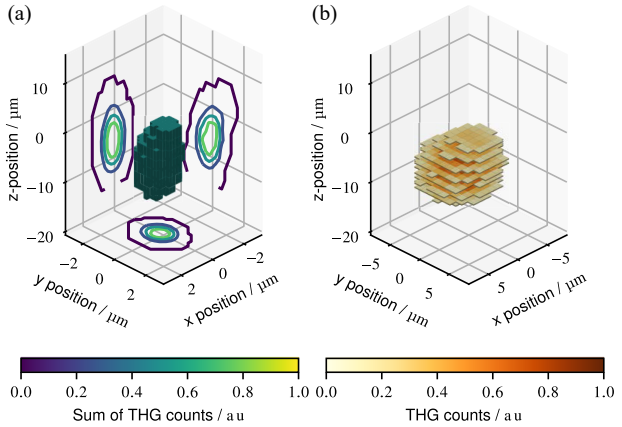

Fig. 3. Comparison between scanning and tomographic acquisition modes of third-harmonic generation (THG) images, while probing an in-volume laser-induced modification ($F = 9.72\ \mathrm{J\ cm^{-2}}$, $n = 14$ pulses). (a) The scanning mode is represented with a scatter plot and projections over the three main axes. (b) The tomographic mode is represented as stacked layers of full-field images, acquired by moving the probe beam along the center of the affected volume. Note that (a) and (b) have different horizontal axis scales.

In the sequel, we show that both the intensity of the THG signals and the THG fingerprints projected on the sensor are strongly related to processing parameters. As such, they contain useful information for characterizing the inscription process.

B. Full-Field, Third-Harmonic Response of Laser-Affected Zones

We first examine the differences between conventional polarized-light microscopy with THG imaging. To this end, we consider a laser-written pattern consisting of a matrix of dots, regularly spaced by 3 μm along both axes to avoid cross talk. For each horizontal line, the processing pulse fluence F linearly increases from 3.9 to 7.2 J cm^{-2}, moving from left to right. Along the vertical axis of the matrix, the number of processing pulses n increases geometrically from 1×10^5, from bottom to top. After each laser-modifying exposure step, the same laser probes the produced LAZ, this time with a pulse fluence of 2.3 J cm^{-2}, below the material modification threshold, but sufficient for triggering THG emission. The full-field THG image is then acquired, taking advantage of the inline arrangement of the imaging setup.

Figure 4(a) shows a polarized-light microscope image of the entire experimental matrix. As can be seen, the birefringence gradually increases with both pulse fluence and number of pulses. Figure 4(b) illustrates a corresponding THG signal collection image for comparison. This image is obtained by scanning the laser beam over the specimen with a scanning step of 0.5 μm. At each step, the THG signal is computed by summing *the entire* THG fingerprint collected on the imager. For this particular case, the imager operates like a large photodetector with high sensitivity, and as such, resembles what a photo-multiplier tube (PMT) or like would produce. However, unlike a single point photodetector, the full-field imager also produces a full frame (320 pixels × 240 pixels) about every 10 ms. As will be seen later on, these patterns contain additional useful information for interpreting laser-induced modifications.

Figure 4(c) shows a few selected examples of full-field THG images acquired by the imager for selected LAZs on the laser-parameters map. These images show different patterns. For a fixed fluence of 9.1 J cm^{-2}, when increasing the number of pulses (and hence the exposure dose), the overall signal (defined as the sum of the THG counts of all pixels on the image) first increases, then does not only reduce, but its fingerprint also spreads over a larger area. This complex behavior is not revealed with conventional microscopy images, and is similar to the behavior observed when examining certain functional properties of LAZs as will be discussed later on [25].

C. Third-Harmonic Response of Modifications to Different Polarization States

In Fig. 4(b), we consider only the case of $\vec{E}_{\mathrm{pump}} \parallel \vec{E}_{\mathrm{probe}}$. However, as parametric conversion processes are strongly polarization dependent, and since we are investigating anisotropic structures (e.g., nanogratings), changing the polarization state of the probe is likely to yield useful information about the LAZs. For instance, THG with circularly polarized light prevents enhancement by optical interfaces within the probe volume [26–28], while linearly

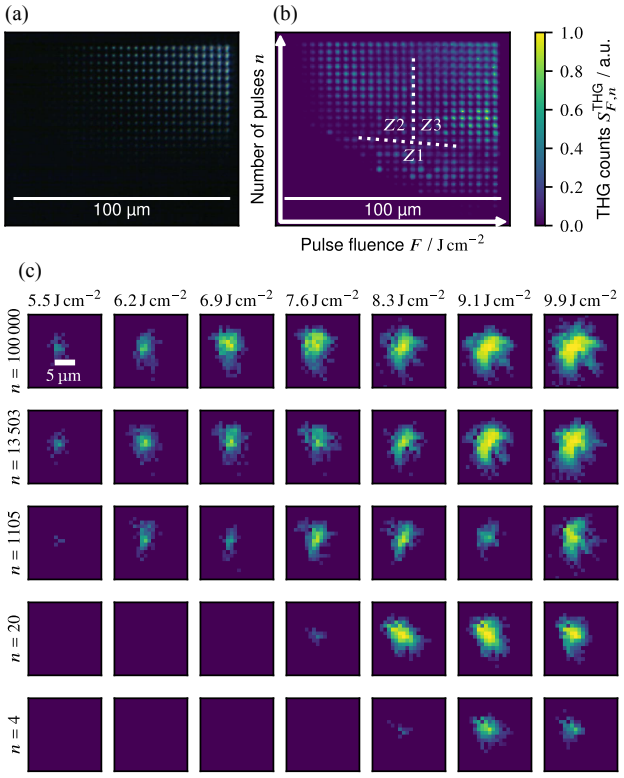

Fig. 4. Full-field third-harmonic generation (THG) microscopy versus polarized-light microscopy images of a matrix of femtosecond laser-affected dots. The full experimental matrix is 80 µm × 70 µm. The axes also correspond to specific exposure conditions. (a) Polarized-light microscopy image of the full matrix of laser-affected dots; (b) same matrix, but with a reconstructed scanning THG microscopy image of the whole processed area, taken at focal depth $\Delta z = 0$ µm, with a scanning step of 0.5 µm. Each point is the sum of all pixel intensities obtained at a given location. The false colors are mapped to the summed THG signals linearly, and normalized over the whole map. (c) Selection of full-field THG images as seen by the imager, normalized to their overall maximum. The top-left image shows a scale bar, using the calibrated resolution of 1 pixel/µm.

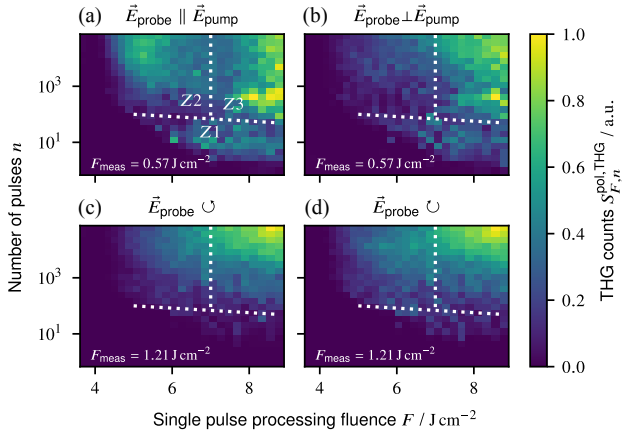

Fig. 5. Matrix representation of the sum of the third-harmonic generation (THG) signals acquired in a full-field image for laser-affected spots in fused silica, obtained for increasing single pulse fluence and number of pulses, and probed using four different polarization states. The observed specimen is the same as in Fig. 4. (a), (b) Case of linear polarization states, parallel and perpendicular, respectively, as defined with respect to the polarization state of the beam that wrote the patterns. (c), (d) Left-handed, right-handed circular polarization states, respectively. The processing peak fluence is indicated on the horizontal axes, and the number of pulses on the vertical one. The pulse fluence used to trigger THG signals is indicated at the bottom of each plot. The value is set so that maximum contrast is achieved, and consequently, circularly polarized probe maps are acquired with higher values compared to linearly polarized ones. Circularly polarized maps (c), (d) appear homogeneous, increasing in signal with both fluence and number of pulses, similar to what is observed under polarized-light microscopy [see Fig. 4(a)]. On the contrary, linearly polarized maps (a), (b) appear heterogeneous, with peaks and valleys of signal. To facilitate the discussion between similarities and differences among polarization states in the main text, we highlight three typical domains, Z1, Z2, and Z3, as shown in (a).

polarized light may enhance THG at a specific orientation, such as that of self-organized nanogratings.

Figure 5 shows the THG signal maps of modifications in fused silica for four different polarization states: parallelly (a) and perpendicularly (b) polarized with respect to the processing beam ($\vec{E}_{pump}$, itself linearly polarized); and (c) left- and (d) right-handed circular polarization, respectively. Compared to Fig. 4(b), we acquire here only the THG signal at the center of each dot, instead of a whole scan. Note that since THG is less efficient using circularly polarized light, the probing pulse fluence intensity is increased to 1.21 J cm^{-2}, compared to 0.57 J cm^{-2} in the linear cases.

In Fig. 5, each square corresponds to the sum of the total THG signal acquired for each single full-field THG image at a given pulse fluence and number of pulses. We observe well-defined boundaries, below which no THG signal is detected. We formulate the hypothesis that a law of incubation, commonly used in ablation studies, describes this phenomenon, as further discussed in Section 3.E.

Circular and linear polarization maps display significant differences. Circular polarization maps show a rather uniform, gradually increasing THG intensity with both fluence and number of pulses. Linear polarization maps show non-uniform distributions, with peaks and valleys. Distinctive regions of interest can be seen in the linear polarization maps, separated by valleys of less intense THG signals. To facilitate the discussion, we refer to them as Z1, Z2, and Z3. Note that all three regions appear in (a), where they are annotated.

Comparing maps in Fig. 5, linear states (a), (b), versus circular states (c), (d), we identify a few-pulse regime (Z1), revealed only with linear polarization, and with higher contrast in case (a). A vertical valley at circa 7 J cm^{-2} separating regions Z2 and Z3 is revealed under both linear polarization states, but is not discernible in circular polarization. We assume that the presence of well-defined nanogratings here significantly enhances the signal for the fitting polarization state, here, $\vec{E}_{pump} \parallel \vec{E}_{probe}$. Nonetheless, the existing underlying signal in the $\vec{E}_{pump} \perp \vec{E}_{probe}$ case implies the presence of other modifications that enhance THG.

The differences among the four THG maps, probed with different polarization states, are interpreted as follows. Region Z1 corresponds to a regime where nano-pores appear, without clearly defined self-organization. These parameters are similar to a regime referred to as "type X" [7], in which oblong nano-pores are found in a relatively homogeneous distribution in the focal spot. This regime bears anisotropy expressed in a weak polarization-dependent retardance level. Interestingly, we notice that the THG

signal there is slightly more intense for a polarization state corresponding to a probe polarization aligned with that of the pump (a). This may be explained by the oblong shape of nano-pores.

Region Z2 is a regime for which strongly anisotropic and well-formed nanogratings appear [3,5]. These nanostructures correspond to self-organized nano-planes, parallel one to another. A clear and distinct THG signal is observed for this particular regime that, in our opinion, can be associated with the strongly anisotropic nature of the nanogratings.

Region Z3, finally, is a regime of higher fluence and greater number of pulses, where disrupted laser-modified zones are forming, typically taking the form of less-organized nanogratings [24,29] and ultimately chaotic structures with a significant number of micro-cracks. We notice a "hot spot" in the lower part of this region.

For all three regions, the THG signal induced by a circularly polarized probe simply gradually increases with both number of pulses and their fluence, and independently of self-organization in LAZs. This behavior follows the birefringence increase as illustrated in Fig. 4(a). This is confirmed in Ref. [27]: optical heterogeneity does not enhance THG emitted under circularly polarized light.

The mechanism leading to THG with a linearly polarized probe is driven by sharp discontinuities in refractive indices, and hence interfaces. In our laser-modified zones, such interfaces are found due to the presence of nano-pores and/or nanogratings and/or cracks, which can be randomly distributed. A THG efficiency peak appears depending on the preferred direction (see region Z2, i.e., nanogratings aligned perpendicularly to the polarization of the processing beam). Strong birefringence allows THG through phase matching—as seen in the case of circularly polarized light.

These observations show that full-field, polarization-resolved THG signals carry useful information that can be directly correlated to the state of matter in LAZs. As such, it can potentially be used as a feedback signal for achieving a desired material structure. In the next section, we explore further the link between full-field THG information and functional properties by correlating THG signals with the chemical etching efficiency of LAZs.

D. Correlation of THG Signal with the Wet Etching Rate in Fused Silica

It is known that the nanogratings' orientations, and consequently, the polarization state of the laser that created them, influence the etching rate of fused silica [30]. Furthermore, an optimal net fluence for achieving the highest rate exists [25]. In this context, THG sensing can help us in identifying laser-parameter zones with the highest etching efficiency.

To investigate the correlation between etching rate and the emitted intensity of THG, we inscribe lines whose parameters are similar to the points inscribed in the last experiment. While the pulse fluence is a fixed quantity, we have to match the number of pulses n with an equivalent scanning speed v_{scan} to compare the two datasets. The conversion formula can be written as $v_{\mathrm{scan}} = f_{\mathrm{rep}} w_0 / N$, with f_{rep} and w_0 as the pulse repetition rate and the spot size at focus, respectively. Due to technical limits related to the maximum velocity of the moving stages, we narrow down the etching study to attainable scanning speeds from 0.03 to 12.9 mm s^{-1} (which corresponds to an equivalent range of 4126 to nine pulses for a single dot), using a pulse repetition rate of $f_{\mathrm{rep}} = 50$ kHz. Each line is written twice, once with the polarization direction parallel to the scanning direction $\vec{E} \parallel \vec{v}$, and once with both being perpendicular to one another $\vec{E} \perp \vec{v}_{\mathrm{scan}}$.

Lines are inscribed across the entirety of a 25 mm × 25 mm × 0.25 mm fused silica sample, on separate, motor-driven stages. This sample is wire-sawn into three pieces, and two of them are wet-etched. The first one is etched in a solution of 2.5 vol% hydrofluoric acid (HF) at room temperature for 3 h. The second part is etched with a 5 vol% solution of caustic soda (NaOH), heated up to 90°C, for 3 h. The third part is left un-etched. The lengths of the etched channels are then measured under a bright-field microscope.

Figure 6(b) reports the etching rate map in the background for NaOH etching with perpendicular polarization. Above it is a contour plot of the corresponding THG signal [cf. Fig 5(a)]. A very clear correlation between the two quantities is observable: they both peak at approximately ($F = 7$ J cm^{-2}, $n = 20$ pulses). The etching peak is slightly offset to the bottom-right of the THG peak, although this can be attributed to the difference in dynamics between static (dots) and translating exposures. Below are reported the etching rates for three other conditions, namely, with parallel polarization using NaOH, and using HF, with both linear polarization directions. Using NaOH, the same peak is reported for both polarization states. In the case of parallel polarization, the etching rate quickly collapses out of this peak region, while it drops roughly two-thirds with more pulses in the other case. With HF, the same behavior regarding polarization is reported, although the peak is much less contrasted to other etching regions.

The greater numbers of pulses show enhanced etching rates for a polarization perpendicular to the scanning direction. In such cases, nanograting-driven selective etching seems to be the favored explanation. For few pulses, however, this anisotropy vanishes, and values for the same etchant become relatively similar: approximately 105 and 45 $\mu\mathrm{m/h}^{-1}$ for NaOH and HF, respectively. This behavior could be explained by the presence of molecular defects, related to recent reports regarding mechanisms leading to laser-induced selective etching [31]. The isotropic behavior at the THG peak has also been recently reported [32]. However, there is no known laser-induced molecular defect in laser-exposed fused silica that could exhibit third-order resonance at 3.6 eV [33]. Considering the spreading of the THG fingerprint reported above, THG most likely comes from optical heterogeneity (e.g., originating from the presence of nano-pores or nanogratings). Both observations are nonetheless not mutually exclusive: molecular defect formation is suspected to be a key step towards nano-pore formation [7]. In the region exhibiting high etching selectivity, both defects and pores may coexist, albeit this phenomenon is mostly carried by the former.

E. Modification Threshold Frontier Modeling

This empirical rule states that in the case of surface ablation, the threshold fluence F_{th} for several materials can be related to the number of pulses N to the exponent of a free parameter S, with $0 < S < 1$, according to [34,35]

$$F_{\mathrm{th}}(N) = F_\infty + (F_0 - F_\infty) N^{S-1}, \tag{1}$$

where F_0, F_∞ are the threshold fluence values for the first incoming pulse and for an infinitely high number of pulses, respectively.

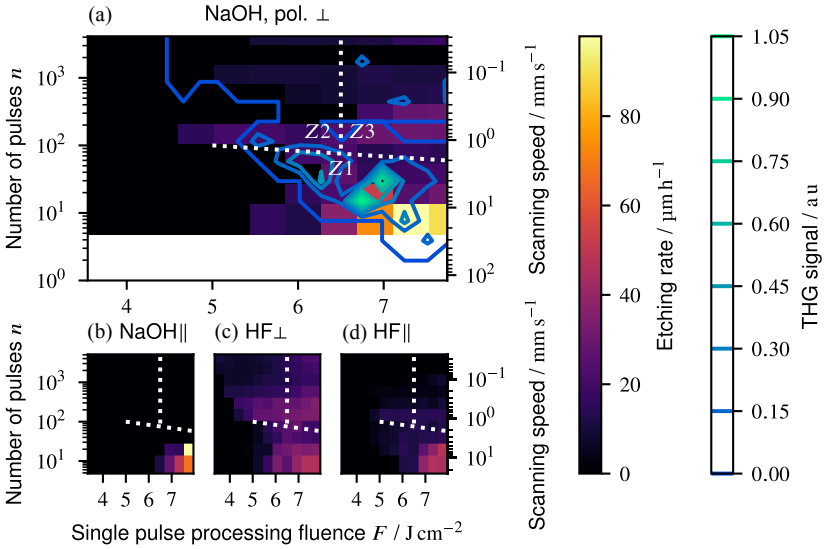

Fig. 6. Comparison between the signal from third-harmonic generation (THG) microscopy of laser-affected spots and the etching rate of lines inscribed using equivalent exposure parameters. The exposed material is fused silica that has been then wet-etched. Several lines of different exposure parameters are inscribed in a single substrate, which is then diamond-wire cut. One part has been etched in a solution of 2.5% HF at room temperature for 3 h, while another has been etched with a 5% solution of caustic soda (NaOH), heated up to 90°C, for 3 h. The lengths of the etched lines are measured to deduce the etching rate. In the backgrounds, maps show the measured values of the etching rate, as a function of the pulse fluence and the relative density of pulses, for each solution, and orientation of $\vec{E}$ relative to the scanning direction. The plotted contours represent the topology of the THG signal for equivalent parameters. A strong correlation between the THG signal and etching rate is observed at low numbers of pulses and high pulse fluence ($\simeq$10 pulses at 340 nJ).

Here, we postulate that this empirical law also applies to the case of bulk modifications. To identify the parameters of this law, we expose several dots, and we measure for each the THG signal after each processing pulse n. We discretize 27 processing fluence values F ranging $6.5 - 9.8\,\mathrm{J/cm^{-2}}$. For statistical reliability, we repeat each experimental data point 24 times, $i \in \{0, 1, \ldots, 23\}$. For every point, we obtain a list containing the sum of the signal over the whole sensor array $S^{\mathrm{THG}}_{F,i}[n] = \sum_{\forall x,y} s_{F,i}[n; x, y]$. Each element of the list corresponds to the THG signal probed after processing with n accumulated pulses. If the signal reaches a detection threshold $S^{\mathrm{THG}}_{\mathrm{th}}$ after a given number of pulses $n < 100$, we define the experimental threshold number of pulses $n_{\mathrm{th}}[F, i] = \min\{n \text{ if} S^{\mathrm{THG}}_{F,i}[n] > S^{\mathrm{THG}}_{\mathrm{th}}\}$. This detection threshold is determined based on the overall noise on the detector. If after 100 pulses the signal remains below this detection threshold, we consider that there is no modification. The data point is therefore skipped, and $n_{\mathrm{th}}[F, i]$ is undefined (as $n_{\mathrm{th}}[F, i] = \min(\emptyset)$).

For each fluence value, we can therefore determine a mean value $\overline{n_{\mathrm{th}}}$ and a standard deviation $\sigma(n_{\mathrm{th}})$. These values are fed into a Levenberg–Marquardt curve-fitting algorithm [36] with the aforementioned incubation law on Eq. (1), to identify parameters F_∞, F_0, and S.

Figure 7 reports the results. The curve-fitting algorithm returns the following parameters for fused silica: $F_0 = 5.1 \pm 0.1\,\mathrm{J/cm^{-2}}$, $F_\infty = 9.0 \pm 0.4\,\mathrm{J/cm^{-2}}$, $S = 0.51 \pm 0.07$. The empirical law of incubation for ablation, as presented in Eq. (1), fits well with the measured THG threshold, and as such can be used as a tool for predicting accurately thresholds for modifications occurring in the material. However, according to previous reports for ablation on fused silica surfaces [37], the fluence threshold for pulses at $\tau_p = 150$ fs and $\lambda = 1030$ nm reaches $F \simeq 3\,\mathrm{J/cm^{-2}}$. Our results are threefold higher. Given that we consider in-bulk exposure, such an increase is intuitive, as the boundary conditions indeed differ from the surface ablation case.

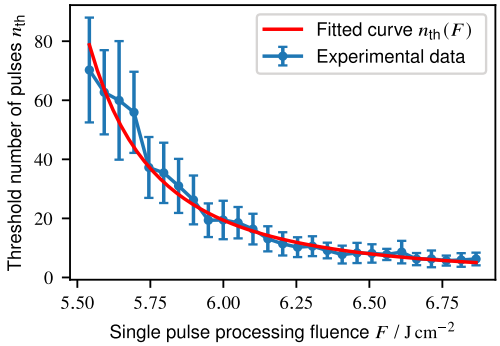

Fig. 7. Measured threshold of laser-induced modifications with direct observation of third-harmonic generation. Average experimental points $\overline{n_{\mathrm{th}}}$ are reported with their associated error bars $\sigma(n_{\mathrm{th}})$ in blue. The data are fitted with the incubation law $F_{\mathrm{th}}(N) = F_\infty + (F_0 - F_\infty)N^{S-1}$, in red.

Interestingly, the observed standard deviation $\sigma(n_{\mathrm{th}})$ decreases with increasing pulse fluence, up until the point where any pulse of a given fluence systematically leads to modifications observable by THG. This observation highlights a relationship between THG signal strength and the occurrence of a physical phenomenon of statistical nature. Events of this kind could be, for instance, crack formation (analyzed with a Weibull distribution) or nano-bubble nucleation events (governed by an exponential growth according to Gibbs theory).

Here, we perform a reliability analysis on the experimental values of thresholds. Assuming the threshold values $n_{\mathrm{th}}[F, i]$ follow a random variable $X(F)$, out of several types of distribution considered, a log-logistic distribution constitutes the best fit [38]. Its probability density PDF_X and its cumulative density CDF_X functions are described as follows:

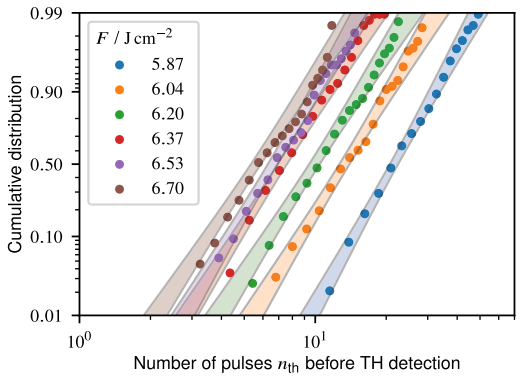

Fig. 8. Log-logistic plot of the measured threshold values. Datasets, here differently colored, are acquired using six different fluence values in the interval of 5.87 to 6.70 J cm^{-2}. The cumulative histogram and the cumulative function of the log-logistic distribution are then fitted to the data. Measurements are reported with dots, and the 95% confidence range of the fitted distributions with lines. The x axis has a log-scale, while the y axis is scaled so that the log-logistic distributions are reported as lines.

$$\mathrm{PDF}_X(n_{\mathrm{th}};\lambda,k)=\frac{(k/\lambda)(n_{\mathrm{th}}/\lambda)^{k-1}}{\left(1+(n_{\mathrm{th}}/\lambda)^k\right)^2}, \tag{2}$$

$$\mathrm{CDF}_X(n_{\mathrm{th}};\lambda,k)=\frac{1}{1+(n_{\mathrm{th}}/\lambda)^{-k}}, \tag{3}$$

with $\lambda>0$ and $k>0$ being the shape and scale parameters of the distribution, respectively. There, we consider both parameters to be dependent on pulse fluence F.

To test the suitability of this law in this particular case, we conducted the same experiment as before. There, we arrange all values of $n_{\mathrm{th}}[F,i]$ into a weighted cumulative histogram. They are then fitted using Eq. (3), and plotted using a reliability analysis library [39].

Figure 8 reports the experimental cumulative distribution data, and the fitted log-logistic distribution $X(F)$. Table 1 reports the optimized distribution parameters, as well as the mean $E(X)\sim\overline{n_{\mathrm{th}}}[F]$, median $Q_{50\%}(X)\sim\mathrm{median}(n_{\mathrm{th}}[F])$, and standard deviation $\sigma(X)\sim\sigma(n_{\mathrm{th}}[F])$. While the shape parameter k barely varies (reported values range over 4.7 to 5.6), the scale factor λ varies negatively with fluence. The quantile function of this distribution writes $Q_p(X)=\mathrm{CDF}_X^{-1}(p;\lambda,k)=\lambda(p/(1-p))^{1/k}$. The median of the log-logistic distribution is therefore equal to its shape parameter $Q_{50\%}(X)=\lambda(F)$. We can therefore estimate the number of pulses needed for to get a 99% chance to generate a defect $Q_{99\%}(X)$, also reported in Table 1.

The log-logistic distribution used here has notably been developed and used as a more robust variation of Weibull distribution [40], especially in the case of censored data [38]. In our case, we terminate experiments after 100 pulses, whether a THG signal is detected or not. We deemed this choice optimal for our experimental setup, considering the time requirement for acquiring the data and their statistical relevance. Statistically, the data are therefore right-censored.

4. CONCLUSION AND OUTLOOK

We have addressed the ability of THG microscopy for *in situ* monitoring of femtosecond laser processing of bulk dielectrics. We have specifically shown the following.

- Full-field THG imaging unravels additional information compared to standard scanning THG microscopy, especially in the form of projected THG patterns from the quasi-point source in LAZs. These patterns possibly emerge from laser-induced scattering centers, such as nano-pores. The exact physical origin of this phenomenon is yet to be formalized.
- This method can discriminate regions of different kinds of laser-induced modifications in parameter space (pulse fluence, number of pulses). Thorough study of the full-field THG image yields a hint on the underlying morphology of the modification. A more detailed study comparing the *in situ* measurements with corresponding *postmortem*, destructive observations (e.g., scanning electron microscopy) could bring more precise insights on this matter. Adaptive optics may help quantify the nature of such modifications, possibly in a single shot manner, which could be a significant step in both nonlinear imaging science, and laser processing.
- When examining the threshold at which THG occurs when probing modifications, the measured values follow the general ansatz for an incubation process. We show that the experimental values follow a random variable, described by a log-logistic distribution, whose shape parameter is fixed and whose scale parameter decreases with the pulse fluence. The latter is equal to the median of the observed values.
- In the case of fused silica, we observe a correlation between the THG signal in the high-fluence, few-pulses regime, and laser-induced selective etching rate.

APPENDIX A: SPATIAL RESOLUTION

As a simple example for discussing the spatial resolution of the nonlinear imaging system, we consider that THG is emitted homogeneously in the focal spot of the probe beam. We assume THG is emitted above a certain threshold I_{th}. The condition for THG in the vicinity of the waist of a Gaussian beam therefore writes

Table 1. Fitted Parameters of the Log-Logistic Distribution for the Random Variable $X(F)$ and the Associated Expected Value E(X), Standard Deviation $\sigma(X)$, Median $Q_{50\%}(X)$, and 99% Quantile $Q_{99\%}(X)$

F/J cm^{-2}	λ	k	E(X)	$\sigma(X)$	$Q_{50\%}(X)$	$Q_{99\%}(X)$
5.87	21.6 ± 0.4	5.6 ± 0.3	22.8	7.9	21.6	49.1
6.04	13.3 ± 0.3	5.1 ± 0.3	14.2	5.5	13.3	32.9
6.20	9.9 ± 0.3	4.9 ± 0.3	10.6	4.3	9.9	25.5
6.37	7.2 ± 0.2	4.9 ± 0.3	7.8	3.1	7.2	18.4
6.53	6.6 ± 0.2	5.2 ± 0.3	7.0	2.6	6.6	15.9
6.70	5.6 ± 0.1	4.7 ± 0.2	6.0	2.6	5.6	15.0

$$\frac{I_{\text{th}}}{I_0} < \left(\frac{w_0}{w(z)}\right)^2 \exp\left(\frac{-2r^2}{w^2(z)}\right) \text{ with } w(z) = w_0\sqrt{1+\left(\lambda z/\pi w_0^2\right)^2}, \tag{A1}$$

with r being the distance from the optical axis, z the distance from the waist, I_0 the maximum beam intensity at the waist, w_0 the beam waist, and λ the wavelength. From this equation, we can deduce the lateral and vertical resolutions, which write $r_{\text{res}} = 2\sqrt{(w_0^2/2)\ln(I_0/I_{\text{th}})}$ and $z_{\text{res}} = 2(\pi w_0^2/\lambda)\sqrt{(I_0/I_{\text{th}})-1}$, respectively, and assuming $I_0 > I_{\text{th}}$. Both tend to zero for $I_{\text{th}} \simeq I_0$. Nonetheless, for such a condition, THG emission is negligible, as it is barely over threshold, and grows cubically: $I_{\text{THG}} \propto I_0^3$. Too high intensity will induce breakdown in the material. Assuming $I_0/I_{\text{th}} = 1.2$, we have $z_{\text{res}} = 4.26\ \mu\text{m}$, and $r_{\text{res}} = 0.75\ \mu\text{m}$.

Funding. Schweizerischer Nationalfonds zur Förderung der Wissenschaftlichen Forschung (213521); Innosuisse—Schweizerische Agentur für Innovationsförderung (43798.1 IP-ENG).

Acknowledgment. As part of his Ph.D. work, O.B. designed and conducted the experiments under the supervision of Y.B., who designed the research program. A.K. implemented and characterized the CMOS imager, while A.B. designed the sensor, both under the supervision of C.E., during their stay at EPFL. J.S. provided advice related to THG microscopy and helped for the design of the custom objective. O.B. and Y.B. wrote the draft manuscript. All authors discussed the results and commented on the manuscript. The authors thank Dr. Enrico Casamenti, Gözden Torun, and Dr. Pieter Vlugter for fruitful discussions regarding the results and the experimental design, as well as Dr. Ilia Sergachev for programming the FPGA.

Disclosures. The authors declare no conflicts of interest.

Data availability. Data underlying the results presented in this paper are available in Code 1, Ref. [41], along with codes used to generated reported values and figures.

REFERENCES

1. R. R. Gattass and E. Mazur, "Femtosecond laser micromachining in transparent materials," Nat. Photonics **2**, 219–225 (2008).
2. A. Marcinkevičius, S. Juodkazis, M. Watanabe, M. Miwa, S. Matsuo, H. Misawa, and J. Nishii, "Femtosecond laser-assisted three-dimensional microfabrication in silica," Opt. Lett. **26**, 277–279 (2001).
3. Y. Shimotsuma, P. G. Kazansky, J. Qiu, and K. Hirao, "Self-organized nanogratings in glass irradiated by ultrashort light pulses," Phys. Rev. Lett. **91**, 247405 (2003).
4. Y. Bellouard, A. Said, M. Dugan, and P. Bado, "Monolithic three-dimensional integration of micro-fluidic channels and optical waveguides in fused silica," MRS Online Proc. Libr. Arch. **782**, 63 (2003).
5. E. Bricchi, B. G. Klappauf, and P. G. Kazansky, "Form birefringence and negative index change created by femtosecond direct writing in transparent materials," Opt. Lett. **29**, 119–121 (2004).
6. Y. Bellouard, T. Colomb, C. Depeursinge, M. Dugan, A. A. Said, and P. Bado, "Nanoindentation and birefringence measurements on fused silica specimen exposed to low-energy femtosecond pulses," Opt. Express **14**, 8360–8366 (2006).
7. M. Sakakura, Y. Lei, L. Wang, Y.-H. Yu, and P. G. Kazansky, "Ultralow-loss geometric phase and polarization shaping by ultrafast laser writing in silica glass," Light Sci. Appl. **9**, 15 (2020).
8. O. Bernard and Y. Bellouard, "On the use of a digital twin to enhance femtosecond laser inscription of arbitrary phase patterns," J. Phys. Photon. **3**, 035003 (2021).
9. R. Stoian, K. Mishchik, G. Cheng, C. Mauclair, C. D'Amico, J. P. Colombier, and M. Zamfirescu, "Investigation and control of ultrafast laser-induced isotropic and anisotropic nanoscale-modulated index patterns in bulk fused silica," Opt. Mater. Express **3**, 1755–1768 (2013).
10. K. Bergner, B. Seyfarth, K. A. Lammers, T. Ullsperger, S. Döring, M. Heinrich, M. Kumkar, D. Flamm, A. Tünnermann, and S. Nolte, "Spatio-temporal analysis of glass volume processing using ultrashort laser pulses," Appl. Opt. **57**, 4618–4632 (2018).
11. R. Grigutis, V. Jukna, M. Navickas, G. Tamošauskas, K. Staliunas, and A. Dubietis, "Conical third harmonic generation from volume nanogratings induced by filamentation of femtosecond pulses in transparent bulk materials," Opt. Express **29**, 40633–40642 (2021).
12. Y. Barad, H. Eisenberg, M. Horowitz, and Y. Silberberg, "Nonlinear scanning laser microscopy by third harmonic generation," Appl. Phys. Lett. **70**, 922–924 (1997).
13. B. Weigelin, G.-J. Bakker, and P. Friedl, "Third harmonic generation microscopy of cells and tissue organization," J. Cell Sci. **129**, 245–255 (2016).
14. M. Müller, J. Squier, K. R. Wilson, and G. J. Brakenhoff, "3D microscopy of transparent objects using third-harmonic generation," J. Microsc. **191**, 266–274 (1998).
15. M. D. Young, J. J. Field, K. E. Sheetz, R. A. Bartels, and J. Squier, "A pragmatic guide to multiphoton microscope design," Adv. Opt. Photon. **7**, 276–378 (2015).
16. J. A. Squier and M. Müller, "Third-harmonic generation imaging of laser-induced breakdown in glass," Appl. Opt. **38**, 5789–5794 (1999).
17. A. Jesacher, P. S. Salter, and M. J. Booth, "Refractive index profiling of direct laser written waveguides: tomographic phase imaging," Opt. Mater. Express **3**, 1223–1232 (2013).
18. J. Guan, X. Liu, and M. J. Booth, "Ultrafast laser writing quill effect in low loss waveguide fabrication regime," Opt. Express **26**, 30716–30723 (2018).
19. J. Guan, X. Liu, and M. Booth, "Investigation of structural mechanisms of laser-written waveguide formation through third-harmonic microscopy," Opt. Lett. **44**, 1039–1042 (2019).
20. M. Lancry, B. Poumellec, J. Canning, K. Cook, J. C. Poulin, and F. Brisset, "Ultrafast nanoporous silica formation driven by femtosecond laser irradiation: In the heart of nanogratings," Laser Photon. Rev. **7**, 953–962 (2013).
21. Y. Bellouard, A. Said, M. Dugan, and P. Bado, "Fabrication of high-aspect ratio, micro-fluidic channels and tunnels using femtosecond laser pulses and chemical etching," Opt. Express **12**, 2120–2129 (2004).
22. A. Boukhayma, A. Kraxner, A. Caizzone, M. Yang, D. Bold, and C. Enz, "Comparison of two in pixel source follower schemes for deep subelectron noise CMOS image sensors," IEEE J. Electron Devices Soc. **10**, 687–695 (2022).
23. C. B. Schaffer, J. Aus der Au, E. Mazur, and J. A. Squier, "Micromachining and material change characterization using femtosecond laser oscillators," Proc. SPIE **4633**, 112–118 (2002).
24. C. Hnatovsky, R. S. Taylor, P. P. Rajeev, E. Simova, V. R. Bhardwaj, D. M. Rayner, and P. B. Corkum, "Pulse duration dependence of femtosecond-laser-fabricated nanogratings in fused silica," Appl. Phys. Lett. **87**, 014104 (2005).
25. S. Rajesh and Y. Bellouard, "Towards fast femtosecond laser micromachining of fused silica: the effect of deposited energy," Opt. Express **18**, 21490–21497 (2010).
26. G. Wagnière, "Optical activity of higher order in a medium of randomly oriented molecule,". J. Chem. Phys. **77**, 2786–2792 (1982).
27. D. Oron, E. Tal, and Y. Silberberg, "Depth-resolved multiphoton polarization microscopy by third-harmonic generation," Opt. Lett. **28**, 2315–2317 (2003).
28. J. Morizet, G. Ducourthial, W. Supatto, A. Boutillon, R. Legouis, M.-C. Schanne-Klein, C. Stringari, and E. Beaurepaire, "High-speed polarization-resolved third-harmonic microscopy," Optica **6**, 385–402 (2019).
29. A. Champion, M. Beresna, P. Kazansky, and Y. Bellouard, "Stress distribution around femtosecond laser affected zones: effect of nanogratings orientation," Opt. Express **21**, 24942–24951 (2013).
30. C. Hnatovsky, R. S. Taylor, E. Simova, V. R. Bhardwaj, D. M. Rayner, and P. B. Corkum, "Polarization-selective etching in femtosecond laser-assisted microfluidic channel fabrication in fused silica," Opt. Lett. **30**, 1867–1869 (2005).
31. E. Casamenti, S. Pollonghini, and Y. Bellouard, "Few pulses femtosecond laser exposure for high efficiency 3D glass micromachining," Opt. Express **29**, 35054–35066 (2021).
32. M. Ochoa, P. Roldán-Varona, J. F. Algorri, J. M. López-Higuera, and L. Rodríguez-Cobo, "Polarisation-independent ultrafast laser selective etching processing in fused silica," Lab Chip **23**, 1752–1757 (2023).
33. L. Skuja, "Optical properties of fused silica," in *Defects in SiO2 and Related Dielectrics: Science and Technology*, Vol. **2** of NATO Science Series II NATO ASI School on SiO2 (Kluwer Academic, 2000), pp. 73–116.

34. D. Ashkenasi, M. Lorenz, R. Stoian, and A. Rosenfeld, "Surface damage threshold and structuring of dielectrics using femtosecond laser pulses: the role of incubation," Appl. Surf. Sci. **150**, 101–106 (1999).
35. Z. Sun, M. Lenzner, and W. Rudolph, "Generic incubation law for laser damage and ablation thresholds," J. Appl. Phys. **117**, 073102 (2015).
36. P. Virtanen, R. Gommers, T. E. Oliphant, M. Haberland, T. Reddy, D. Cournapeau, E. Burovski, P. Peterson, W. Weckesser, J. Bright, and S. J. WaltDerVan, "SciPy 1.0: fundamental algorithms for scientific computing in Python," Nat. Methods **17**, 261–272 (2020).
37. B. Chimier, O. Utéza, N. Sanner, M. Sentis, T. Itina, P. Lassonde, F. Légaré, F. Vidal, and J. C. Kieffer, "Damage and ablation thresholds of fused-silica in femtosecond regime," Phys. Rev. B **84**, 094104 (2011).
38. S. Bennett, "Log-logistic regression models for survival data," Appl. Stat. **32**, 165 (1983).
39. M. Reid, "MatthewReid854/reliability: v0.5.1," version v0.5.1, Zenodo (2020), https://zenodo.org/record/3938000.
40. W. Weibull, "A statistical distribution function of wide applicability," J. Appl. Mech. **18**, 293–297 (1951).
41. O. Bernard, "Supplementary material—algorithms and data," figshare, 2023, https://doi.org/10.6084/m9.figshare.22015220.